Please do not adjust margins

This is the Pre-Published Version.

The following publication Zhuang, L., Zhai, L., Li, Y., Ren, H., Li, M., & Lau, S. P. (2021). Mixed dimensional 0D/3D perovskite heterostructure for efficient green light-emitting diodes [10.1039/D1TC03611D]. Journal of Materials Chemistry C, 9(40), 14318-14326 is available at https://dx.doi.org/10.1039/d1tc03611d.

ARTICLE

Mixed Dimensional 0D/3D Perovskite Heterostructure for Efficient Green Light Emitting Diodes

Received 00th January 20xx,
Accepted 00th January 20xx

DOI: 10.1039/x0xx00000x

Lyuchao Zhuang,[a] Lingling Zhai,[a] Yanyong Li,[a] Hui Ren,[a] Mingjie Li,[a] Shu Ping Lau,*[a]

Metal halide perovskites are emerging materials for next-generation optoelectronic devices, of which all-inorganic $CsPbBr_3$ perovskite has attracted increasing attention due to outstanding stability and excellent photoelectric characteristics compared with organic-inorganic counterparts. However, the electroluminescence (EL) efficiencies of inorganic $CsPbBr_3$ perovskite light emitting diodes (PeLEDs) were unsatisfactory because of high trap densities, leading to non-radiative recombination loss. Herein, by introducing potassium bromide (KBr), we successfully prepare zero-dimensional/three-dimensional (0D/3D) $Cs_{4-x}K_xPbBr_6/CsPbBr_3$ heterostructure perovskite films with suppressed trap density and improved photoluminescence quantum yield (PLQY). The deep energy level of 0D $Cs_{4-x}K_xPbBr_6$ phase is confirmed using DFT calculation. Moreover, the formation of the unique heterostructure inhibits free charge diffusion at the grain boundary from suffering trapping recombination, which facilitates efficient radiative recombination in the 3D $CsPbBr_3$ phase. Therefore, the optimized green PeLEDs shows a high external quantum efficiency (EQE) of 12.8 % which is around six-fold improvement than pristine one (2.1%) and a maximum brightness of 39400 cd m^{-2}. Our work provides a rational charge carrier confinement strategy for developing high-performance PeLEDs and can be broadened to other potential perovskite materials, not restricted in the $CsPbBr_3$-based perovskite films.

Introduction

Metal halide perovskites have attracted extensive attention due to their excellent optical and electrical properties. Moreover, perovskite materials have the advantage of narrow and tunable emission spectra, low-cost and solution processing.[1-3] In recent years, extensive research has been focused on PeLEDs. Especially, significant breakthroughs have been achieved in green PeLEDs. The first green PeLED was demonstrated in 2014 with an external quantum efficiency (EQE) of 0.1% and a maximum luminance of 364 cd m^{-2}.[4] Notably, the performance of PeLEDs has been improved quickly with an EQE of 23.4% using $FA_{1-x}GA_xPbBr_3$ perovskite nanocrystals.[5] Still, the instability and difficulty in large-scale nanocrystals synthesis still restrict its practical application.[6, 7]

The Cs-based all-inorganic halide perovskites, such as $CsPbBr_3$, have been widely used as alternative emitters in PeLEDs due to their outstanding photoelectric characteristics and stability.[8, 9] However, the traditional one-step spin-coating method applies inorganic $CsPbBr_3$ precursor solution without any host materials, leading to non-uniform polycrystalline layers with poor quality.[8] Consequently, the trap densities in $CsPbBr_3$ perovskite are comparable with the charge carrier concentration in the typical PeLEDs operational regime. Moreover, charge carrier delocalization leads to strong trap-assisted non-radiative recombination effects in the grain boundary.[10-12] Thus, manipulating charge carrier recombination dynamics has been found to be the crucial strategy to realize high device efficiencies in PeLEDs. Generally, the charge carrier confinement in the perovskite crystal can be controlled through spatial confinement.[10] The diffusion length can become smaller, and the exciton binding energy can get larger by drastic shrinkage of grain size, which spatially confines the charge carriers within a crystal grain. [8, 13, 14] The reduction of grain size always accompanies an increasing number of grain boundaries, leading to a large degree of surface defects, inevitably. Apart from the aforementioned strategy, constructing a heterophased structure in films has been proven to be the effective method to fabricate stable and high-performance PSCs and PeLEDs.[15, 16] Due to the high crystallinity and good band alignments, the 2D/3D heterojunction effectively suppressed the non-radiative recombination and enhanced the photoelectric performance.[17] Besides, the insulation nature of the bulky organic in the 2D perovskite is also a challenge for efficient charge transport. It has also been reported that the different dimensional Cs-based perovskite can be obtained by controlling the stoichiometry between Cs, Pb and halide (X). [18] Interestingly, 0D perovskites also possess larger exciton binding energy and deeper energy level, which effectively confine the electrons and holes. Recently, a heterostructure comprising 0D Cs_4PbI_6 and 3D γ-$CsPbI_3$ with the excitons confinement is manifested to achieve a stable all-inorganic perovskite solar cell with a high-power conversion efficiency.[19] 0D/3D hybrids can inherit the charge confinement from 0D phase and the

[a] *Department of Applied Physics, The Hong Kong Polytechnic University, Hung Hom, Kowloon 999077, Hong Kong, People's Republic of China*
**Email: apsplau@polyu.edu.hk*
Electronic Supplementary Information (ESI) available: [details of any supplementary information available should be included here]. See DOI: 10.1039/x0xx00000x

Please do not adjust margins

Please do not adjust margins

outstanding optoelectronic properties from 3D perovskites.[20] Therefore, a methodology that would form a 0D/3D multi-phases carriers centralization structure for $CsPbBr_3$-based perovskite and suppress non-radiative recombination for enhanced luminescence quantum yield is a feasible alternative for an efficiency PeLEDs realization.[3, 17, 21, 22]

In this work, we demonstrate the efficient $CsPbBr_3$-based PeLEDs by constructing the carrier centralization structure with in-situ fabrication of 0D/3D perovskite heterostructure tuning the stoichiometry of the precursors between KBr and PbBr. To systematically confirm the existence of 0D $Cs_{4-x}K_xPbBr_6$ phase, grazing-incidence X-ray diffraction (GIXRD), UV-vis absorption and high-resolution transmission electron microscopy (HRTEM) were conducted. Density function theory (DFT) calculation suggests a type I heterostructure can be formed between the 3D $CsPbBr_3$ and the 0D $Cs_{4-x}K_xPbBr_6$ phases, which results in confined excitons and enhanced radiative recombination in 3D phase. The structure can render the PLQY of perovskite film to 35%, which is improved by a factor of 3 compared with the pristine one (10%). Accordingly, the corresponding PeLEDs fabricated yield to the maximum brightness of 39400 cd m^{-2}, a maximum current efficiency of 43.7 cd A^{-1} and a peak EQE of 12.8 %, about 6-fold higher than the control PeLEDs (2.1%). This 0D/3D charge carrier confinement strategy is proven to effectively facilitate radiative recombination, which is expected to boost the PeLEDs device efficiency. These findings further illustrate the feasibility of forming perovskite heterostructure and consequent properties enhancement of the perovskite film, suggesting an alternative direction to fabricate the highly efficient PeLEDs.

Experimental Section

Materials

CsBr (99.999%), $PbBr_2$ (99.999%), KBr (99.999%), DMSO (anhydrous, 99.9%), DMF (anhydrous, 99.9%) were purchased from Sigma-Aldrich. PEO (average Mv=100,000), 18-Crown-6 (99%) were purchased from Macklin. p-F-PEABr was purchased form TCI. PEDOT:PSS AI 4083 was purchased from Heraeus. TPBi (>99%) and LiF were purchased from Lumtec. All the materials were used as received.

Perovskite precursor solutions

CsBr, $PbBr_2$ and p-F-PEABr were dissolved with a ratio of 1.1:1:0.2 in the DMSO/DMF mixture solvent (4:1, by volume), with a concentration of 0.2M, 4mg ml^{-1} PEO and 2mg ml^{-1} 18-Crown-6 were also added. The KBr incorporating concentration was controlled by changing molar feed ratios of K/Pb to be 2.5%, 5.0%, 10%, 15% and 20%. All these perovskite precursor solutions were stirred overnight at 60 ℃ in a nitrogen-filled glove box.

Fabrication of perovskite LED

Pattern ITO-coated glasses were ultrasonically cleaned with deionized water, acetone, and isopropyl alcohol for 15 mins each, and treated with Oxygen Plasma for 15 mins before depositing the PEDOT:PSS films. PEDOT:PSS was spun coat onto the ITO substrates at 3000 rpm for 40 s, and the film was annealed at 150 ℃ for 30 mins in air. The perovskite precursor solutions were spin-coated at 3500 rpm for 60 s, followed by annealing at 80℃ for 10mins. TPBi (40 nm) and LiF/Al electrodes (1 nm/ 100nm) were deposited by thermal evaporation under a high vacuum of 2×10^{-4} Pa. The device area is 4.5 mm^2 by the overlapping area of the ITO and Al electrodes.

Characterization Measurement

Grazing incidence X-ray diffraction (GIXRD) analysis for the crystal structure was obtained by Cu Ka radiation (45 KV, 200 mA, Rigaku SmartLab 9kW), and the incident angle was 0.02°. The ultraviolet-visible absorbance spectra (UV-Abs) of the perovskite films were measured using a Perkin Elmer UV-vis-NIR spectrometer. The photoluminescence spectra (PL) and absolute photoluminescence quantum yield (PLQY) were measured using an Edinburgh Photoluminescence FLS 920 equipped with an integrated sphere. Time-resolved photoluminescence (TRPL) was collected using time-correlated single-photon counting for 10000 counts. Excitation was provided by an Edinburgh EPL-375 nanosecond pulsed diode laser. The PL decay was fit using a triexponential decay function. The morphology was measured from field scanning electron microscopy (FESEM) images were obtained from TESCAN MAIA3. The energy-disperse X-ray spectra (EDX) were investigated by scanning electron microscope (SEM) using a Tescan VEGA3 microscope equipped with X-max5 EDX (Oxford Instruments). The high-resolution transmission electron microscopy (HRTEM) images were obtained using a JEOL JEM-2100F at 200kV. The atomic force microscopy (AFM) image and roughness analysis were obtained with a Bruker NanoScope 8. X-ray photoelectron spectroscopy (XPS) and ultraviolet photoelectron spectroscopy (UPS) were measured on a Thermo Fisher Nexsa. The source was a monochromatic Al Kα (E_{photon} = 1486.6 eV) with a 10 mA filament current and a 12 keV filament voltage. UPS measurements utilized the He (I) photo line (21.22 eV) from a He discharge lamp and the high-binding energy secondary electron cutoff (E_{cutoff}), and the HOMO region data were extracted from the UPS spectra. The HOMO levels could be expressed as HOMO=21.22-(E_{cutoff}-E_Δ) (where E_Δ is the gap between the HOMO level and the Fermi level (E_F). The transient absorption (TA) measurements were performed on a femtosecond (fs) pump-probe system (Helios, Ultrafast System LLC) under ambient conditions. The pump pulses (wavelength: 400 nm, pump fluence: 0.3μJ cm^{-2} $pulse^{-1}$ at the sample surface, spot size: 2 mm) were generated by frequency doubling the 800 nm fs laser from a Ti:sapphire regenerative amplifier (Coherent Libra; 800 nm, 35 fs pulse width, 1 kHz) with a BBO crystal. The white-light probe continuum was generated by focusing the fundamental 800 nm beam from Ti: sapphire laser onto a sapphire plate (2 mm thick). The time delay between the pump and probe pulses was varied by a motorized optical delay line (maximum ≈8 ns).

PeLED characterization

This journal is © The Royal Society of Chemistry 20xx

Please do not adjust margins

Please do not adjust margins

A Keithley 2400 source-meter and a fibre integration sphere (FOIS-1) coupled with a QE Pro spectrometer (Ocean Optics) were utilized. The absolute radiance was calibrated by a standard Vis–NIR light source (HL-3P-INT-CAL plus, Ocean Optics). The EQE and spectral evolution with time was measured using the same system. All the measurements were conducted in ambient air at room temperature and without encapsulation.

DFT Calculation

The DFT calculations were carried out using the Vienna Ab-initio Simulation Package (VASP)[23, 24] with the frozen-core all-electron projector-augment-wave (PAW)[25, 26] methods. The Perdew-Burke-Ernzerhof (PBE)[27] of generalized gradient approximation (GGA) was adopted to describe the exchange and correlation potential. The cut-off energy for the plane-wave basis set was set to 500 eV. For the crystal model, a cell of $Cs_{24}Pb_6Br_{36}$ was adopted with a dimension of 14.06×14.06×17.58 Å. For K-incorporated models, one and three Cs atoms were replaced by K atoms, denoted as $Cs_{23}K_1Pb_6Br_{36}$ and $Cs_{21}K_3Pb_6Br_{36}$, respectively. Especially, three different K positions were considered for the $Cs_{21}K_3Pb_6Br_{36}$. The geometry optimizations were performed until the forces on each ion were reduced below 0.01 eV/Å, and the 3×3×2 k-point[28] sampling of the Brillouin zone was used for all calculations.

Results and discussion

The perovskite films were synthesized through a one-step spin coating method, as shown in Figure1(a). The control films without KBr are referred to as 3D perovskites. For 0D/3D perovskites, a certain amount KBr was incorporated into the perovskite precursor to promote the formation of the 0D $Cs_{4-x}K_xPbBr_6$ phase. The diverse connectivity of PbX_6 octahedron in the three-dimensional space produces diversiform species of perovskites possessing 3D, 2D, 1D, and 0D structures.[29] Figure 1(b) depicts the schematic structures of 3D and 0D perovskite phases. $CsPbBr_3$ phase is a 3D perovskite, where the crystal structure is based on the corner-shared $PbBr_6^{4-}$ octahedra. On the contrary, the Bergerhoff–Schmitz–Dumont-type crystal structure of Cs_4PbBr_6 makes the Cs^+ ions minimize the electronic overlap between adjacent octahedra, resulting in localized states that are confined to the individual octahedra.[30] The energy band structures for the pure 0D Cs_4PbBr_6 and $Cs_{4-x}K_xPbBr_6$ were investigated, Figure 1(c). The energy level of 0D Cs_4PbBr_6 is much deeper than those of 3D $CsPbBr_3$ (conduction band -3.33eV, valence band -5.67eV).[31] Combined with the DFT calculation, the energy level of 0D $Cs_{4-x}K_xPbBr_6$ is also deeper than those of 3D $CsPbBr_3$, confirming the feasibility for 0D $Cs_{4-x}K_xPbBr_6$/3D $CsPbBr_3$ heterostructure formation shown in Figure 1(d). In the 0D/3D heterostructure perovskite, excitons in 0D perovskites are transferred to 3D phase, and free excited charges in 3D perovskite are confined and not diffused into 0D phase due to the limited carrier transfer. Thus, it is hypothesized that radiative recombination in 3D phase would boost due to the increase in electron and hole density for 3D phase in the carrier centralization structure.

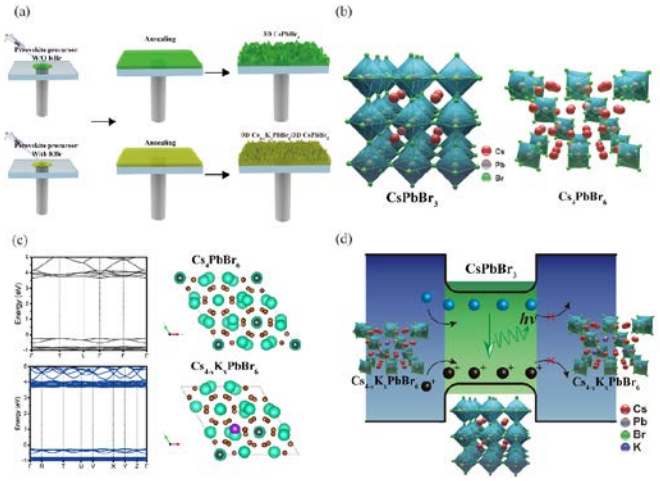

Figure 1. (a) Schematic of one-step spin coating for 3D $CsPbBr_3$ perovskite films and 0D/3D heterostructure perovskite films, (b) The schematic structures of 3D $CsPbBr_3$ and 0D Cs_4PbBr_6 phases (c) The density function calculation for energy band structure of the pure 0D Cs_4PbBr_6 and 0D $Cs_{4-x}K_xPbBr_6$ (d) Carrier recombination diagram of 0D/3D perovskites heterostructure.

GIXRD was conducted to investigate the crystal structure and confirm the formation of 0D/3D perovskite thin films, as shown in Figure 2(a). For easier reference, the perovskite films with different ratios of KBr will be denoted as K2.5%, K5.0%, K10%, K15%, K20% (see the Experimental Section for details). The diffraction peaks located at 15.3°, 21.7°, 30.7°, 34.5°, 37.7°, and 44.1° are assigned to (110), (200), (220), (222), (132), and (040) planes, respectively.[32-34] Commonly, K^+ cation with an intermediate ionic radius (138 pm) can hardly substitute the A-site cation into the perovskite structure.[34] Thus, no diffraction peak shift can be observed in the K^+ incorporation samples, suggesting that K^+ remains outside of the $CsPbBr_3$ perovskite. Furthermore, as the K^+ doping concentration increases, two new peaks at around 13.07° and 29.46° appear simultaneously, demonstrating the formation of 0D phase.[36, 37] The extra CsBr in precursor will combine with parts of $CsPbBr_3$ to form Cs_4PbBr_6 phase structure (Equation (1)).[38] In this work, as the addition of extra KBr is adopted, the newly formed phase is a locally disordered 0D $Cs_{4-x}K_xPbBr_6$ phase (Equation (2)).[32, 36, 39-41]

$$3CsBr + CsPbBr_3 \rightarrow Cs_4PbBr_6 \quad (1)$$

$$(3-x)CsBr + x\ KBr + CsPbBr_3 \rightarrow Cs_{4-x}K_xPbBr_6 \quad (2)$$

The absorption properties of the 3D $CsPbBr_3$ perovskite films and 0D/3D perovskite films were characterized by UV-visible absorption measurement as depicted in Figure 2(b). A slight absorption band was observed around 315 nm stemming from the $^1S_0 \rightarrow {}^3P_1$ transition of Pb^{2+} centres in the Cs_4PbBr_6 0D phase, as has been reported by Nikl and coworkers.[35, 37, 42] The absorption spectra thus further confirm the excess KBr addition contributes to the formation of 0D $Cs_{4-x}K_xPbBr_6$.[41] The observed large bandgap also proves the DFT calculation results and our hypothesis for the carrier centralization structure formation between 3D and 0D perovskite phase.

To better understand the structural changes upon 0D/3D perovskite heterostructure construction, transmission electron microscopy (TEM) along with the Fast Fourier Transform (FFT) for the corresponding area were carried out. The samples for TEM measurement were prepared by spin coating the perovskite precursor on the carbon support copper grids directly. In the control sample (Figure 2c), the interplanar spacing of 2.95Å corresponds to the (200) plane of $CsPbBr_3$.[43] For the K15% 0D/3D heterostructure perovskite film (Figure 2d),

Please do not adjust margins

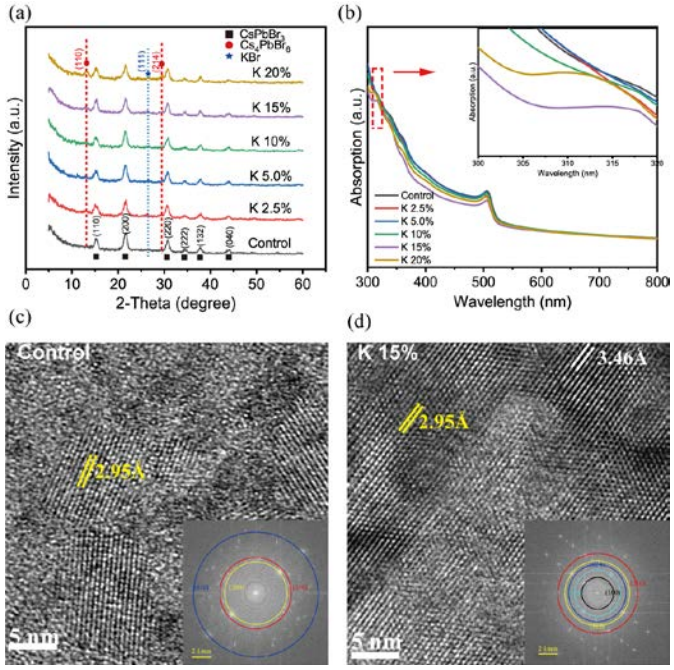

Figure 2. (a) XRD patterns of the $CsPbBr_3$ films and 0D/3D heterostructure perovskite films, (b) UV-vis absorbance spectra of the $CsPbBr_3$ films. Inset the wavelength region between (300 - 320 nm). (c) Control and (d) K15% 0D/3D heterostructure perovskite samples, respectively. Insets are the corresponding Fast Fourier Transform (FFT) images.

the lattice spaces of 2.95Å and 3.46Å can be assigned to the $CsPbBr_3$ (200) and Cs_4PbBr_6 (024) lattice planes, confirmed the existence of different perovskite phases.[32] The FFT result for the control sample shows the diffraction spots corresponding to (200), (210) and (410) planes. For the K15% 0D/3D heterostructure perovskite, the diffraction spots of (100), (110) and (210) planes can be assigned to $CsPbBr_3$. Moreover, diffraction spots corresponding to the interplanar spacing of (312) and (024) planes of 0D phase are also observed. These results further confirmed the coexistence of 3D and 0D phases in the K15% 0D/3D perovskite film.

The morphology of perovskite thin films is another crucial factor governing the performance of PeLEDs. The Field-Emission Scanning Electron Microscopy (FESEM) was used to characterize the morphology of the perovskite thin films. The 3D $CsPbBr_3$ perovskite showed a poor film morphology with a large number of pinholes and cracks compared to 0D/3D perovskite films, Figure 3a. These improvements for film morphology can achieve better charge injection balance and device performance. As seen, the average grain size becomes smaller (Figure S9) for the K15 0D/3D perovskite. Furthermore, benefiting from the construction of 0D/3D heterostructure, it also reduces the RMS roughness of the perovskite films as shown in Figure 3g. Quan *et al.* reported that the cubic $CsPbBr_3$ nanocrystal is satisfied inside a 0D Cs_4PbBr_6 matrix without practical strain on the nanocrystals.[38] Herein, the 0D $Cs_{4-x}K_xPbBr_6$ has the same hexagonal phase as the pure Cs_4PbBr_6. Therefore, combined with the TEM result, the 0D phase might be in situ formed around the 3D $CsPbBr_3$ lattice as a wrapping layer, suppressing the grain growth and passivating the defects in the grain boundary.[19, 44] Those all will contribute to the efficient radiative recombination that will be discussed below.

Normally, this charge carrier confinement structure is an advantage in terms of optical properties. First, the steady-state

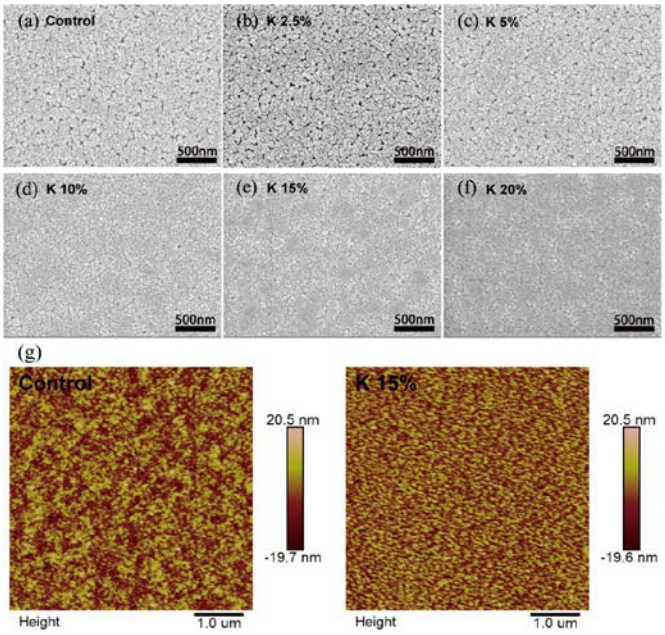

Figure 3. (a)-(f) SEM image of as synthesized CsPbBr3 film. Scale bar: 500 nm. (g) AFM image of control $CsPbBr_3$ (left) and K15% 0D/3D heterostructure (right) film. Scale bar: 1 μm.

photoluminescence (PL) spectroscopy technique was performed on the as-synthesis 3D and 0D/3D $CsPbBr_3$ perovskite films. Figure 4a shows that all the perovskite films exhibited intense and narrow PL spectra that peaked at around 520 - 530 nm. The reduced domain size of the perovskite crystallites is also evident from the blue-shift PL peaks. The steady-state PL intensity increases as the KBr amount increases from 0 to 15% with respect to $PbBr_2$. The PLQY of the as-synthesis $CsPbBr_3$ perovskite films was measured following the method reported by de Mello et al. to determine the influence of the charge carrier confinement.[45] Surprisingly, in $CsPbBr_3$ perovskite film with 15% KBr addition forming the 0D/3D perovskite heterostructures, the PLQY of ~35% is obtained, which is over two times larger than that of the control sample as depicted in the inset of Figure 4a. In general, the nonradiative recombination centres are concentrated around the defects in the grain boundaries. Thus, the films with large grain sizes should have better optical performance due to the fewer grain boundaries. However, the as-synthesized films with smaller grain sizes possess a higher PL intensity and PLQY. These results imply that the defects effectively passivated in the grain boundaries benefiting from the 0D $Cs_{4-x}K_xPbBr_6$ phases surrounding the $CsPbBr_3$. After light or electrical excitation, the electrons and holes in 0D phase are partially transferred to the narrower bandgap domain due to the energy transfer channels in the 0D/3D perovskites heterostructure. The density of electrons and holes in the 3D domain can be increased, thus resulting in enhanced PL emission.[31, 46]

Next, time-resolved PL (TRPL) measurement was conducted to obtain more insight into the radiative and non-radiative recombination process in the 0D/3D $CsPbBr_3$ perovskite films. The longest emission lifetime (with an average lifetime of 83.4 ns) was observed in K15% 0D/3D heterostructure perovskite sample, as shown in Figure 4b and Table S1. The prolonged carrier lifetimes for 0D/3D perovskite films could be due to the reduced trap density and suppressed non-radiative recombination, which agree well with the increased PL intensity as mentioned before. See Table S1, the fraction of τ_2 (A_2)

This journal is © The Royal Society of Chemistry 20xx

Please do not adjust margins

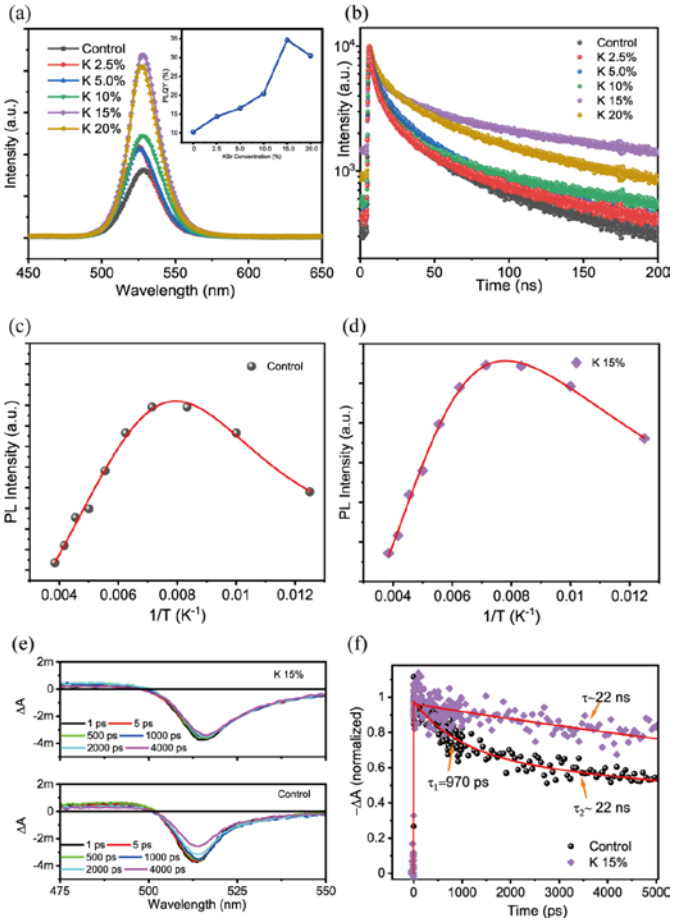

Figure 4. (a) PL spectra (inset the PLQYs) and (b) PL lifetimes of the 3D $CsPbBr_3$ perovskite films and K15% 0D/3D heterostructure perovskite films. (c) and (d) Temperature-dependent of the integrated PL intensity of the 3D $CsPbBr_3$ and K15% 0D/3D heterostructure perovskite film. The solid red curves are the fitting results based on the exciton-trap model. (e) TA spectra and (f) dynamics (probed that the peaks of bleaching) of the 3D $CsPbBr_3$ and K15% 0D/3D heterostructure perovskite film.

decreases first and then increases with the increase of KBr amount. At the same time, the trend of the fraction of τ_3 (A_3) is opposite to that of A_2. The declined A_2 indicates less trap-assisted recombination at grain boundaries, suggesting that the formation of 0D phase can effectively passivate defects, thus the charge capture by defects can be reduced. The increased A_3 manifests more radiative recombination inside the 0D/3D perovskite, ultimately contributing to EL efficiency. A large number of free charge diffusion in the 3D perovskite is suppressed and recombined with the opposite charge remaining in the grain for the recombination. Thus, the charge confinement increases the opportunity of electron and hole recombination, enhancing the radiative recombination in 3D phase for emission.[22] It proved that the formation of 0D/3D mixed dimensional perovskite heterostructure, can remain the charge in 3D phase and not suffer from trapping at the grain boundaries, which facilitates more efficient radiative recombination in 3D phase.

The evolution of PL intensity with temperature can reflect the stability of the photogenerated excitons. Figure 4c, d plots the integrated PL intensity as a function of temperatures for the 3D $CsPbBr_3$ and K15% 0D/3D perovskite film samples. As the temperature decreases from 300 K, the integrated PL intensity first increases, followed by a decrease as the temperature further reduces. More intense PL is expected at a lower temperature, benefiting from the suppressed phonon-assisted non-radiative recombination.[47] Thus, a reduction in the PL intensity at a lower temperature is rarely observed. The negative thermal quenching phenomenon mechanism has been explained by shallow trap states located near the edge of the bandgap. The corresponded exciton binding energy (E_j) is extracted through a combined exciton-trap model[48, 49]:

$$I(T) = I_0 \frac{1+D_1 \exp\left(-\frac{E_q}{k_B T}\right)}{1+C_1 \exp\left(-\frac{E_j}{k_B T}\right)} \qquad (1)$$

where I_0 represents the intensity at 0K, $I(T)$ is the integrated PL intensity at a finite temperature, k_B is the Boltzmann constant, and E_j is the exciton binding energy, E_q is the ionization energy of the trap state. Parameter D_1 and C_1 are proportionality factors. The detailed fitting parameters are shown in Table S2. The fitted exciton binding energies E_j of the 3D $CsPbBr_3$ perovskite and K15%, 0D/3D heterostructure perovskite films are 56.36 and 64.20 meV, respectively. The K15% 0D/3D heterostructure perovskite films possess higher exciton binding energies, which is expected to achieve better performance PeLEDs.[30]

Further, transient absorption (TA) was used to investigate the effect of the non-radiative defect states on the recombination dynamics in our $CsPbBr_3$ and K15% 0D/3D $CsPbBr_3$ heterostructure perovskite films, Figure 4e. Both TA spectra show an identical negative signal at around 516 nm, corresponding to the exciton blenching. Compared with the control sample, the dynamic of blech recovery for the K15% 0D/3D heterostructure perovskite film sample is much slower, indicating the excitons are less likely to be trapped by the defects. Furthermore, the transition dynamics for bleach peaks of the 3D and 0D/3D perovskites were compared (Figure 4f), also demonstrating the reduction of the defect. This result is consistent with TRPL observations that radiative recombination for luminescence is enhanced. Also, to evaluate the defect state of the 3D $CsPbBr_3$ and 0D/3D heterostructure perovskite films,

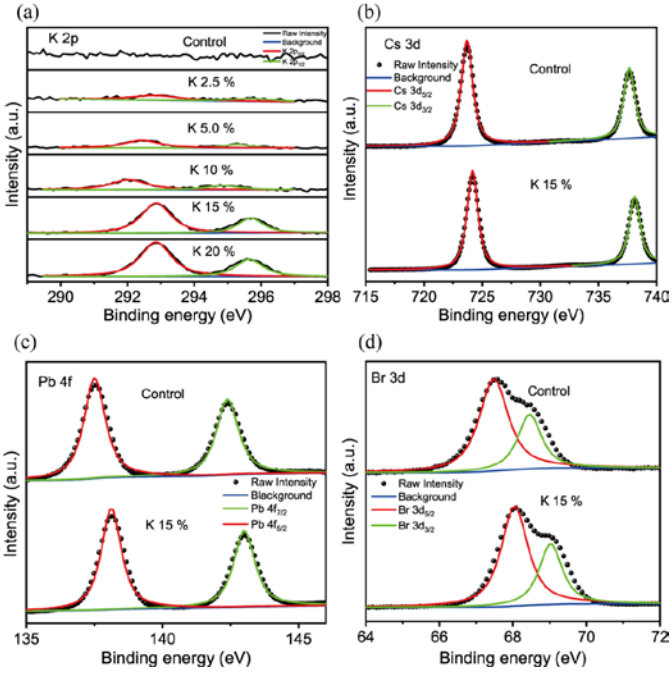

Figure 5. (a)-(d) XPS characterization. High-resolution XPS spectra of the control- (3D CsPbBr3) and K15%- (0D/3D heterostructures) perovskite films for (a) K 2p, (b) Cs 3d, (c) Pb 4f and (d) Br 3d elements, respectively.

Please do not adjust margins

Please do not adjust margins

a space-charge-limited-current (SCLC) method was employed by fabricating hole-only devices in the structure of ITO/PEDOT:PSS/Perovskite/MoO_3/Ag, Figure S8. The trap density of K15% 0D/3D perovskite thin films is estimated to be 6.800×10^{17} cm^{-3}, which is lower than 3D perovskite (1.079×10^{18} cm^{-3}). The reduction in trap density is in accordance with the above TRPL and TA observation.

X-ray photoelectron spectroscopy (XPS) measurements were performed to identify the composition and chemical states of the as-synthesis perovskite films. The spectra were calibrated using the maximum of the adventitious C 1s signal at 284.8 eV. The presence of K was confirmed from the deconvolution of K 2p XPS spectra, Figure 5a. Two different peaks centred at around 292.5 eV and 295.5 eV are observed, corresponding to K 2p3/2 and K 2p1/2 groups, respectively. Obviously, no characteristic peaks of K are detected in the spectra of the control sample. The intensity of K 2p peaks also increases with the content of K, which can also be determined by the atomic ratios of Cs to K derived from the XPS spectra. It is noteworthy that the XPS peaks of K shift to lower binding energy direction in the low-dose KBr incorporation samples. However, when the concentration of KBr is above 15%, the XPS peaks of K 2p shift to the higher binding energy direction. We suppose that the further increase of KBr addition may lead to a more unreacted KBr phase. And the unreacted KBr possess the higher K 2p3/2 and 2p1/2 binding energy around 292.9 eV and 295.8 eV, respectively.[50] Thus, it will cause the binding energy of K 2p to slightly shift to the higher binding energy direction. Interestingly, distinct peaks shift in binding energy was also observed in the case of Cs 3d (0.6 eV), Pb 4f (0.6 eV), and Br (0.5 eV), comparing to the K15% 0D/3D heterostructure perovskite film sample, Figure 5b, 5c and 5d. The shifts in binding energy are clear evidence for the change in chemical bonding properties between cations and anions after 0D/3D perovskite heterostructure construction. Phase stability of the perovskites is determined by the volumetric ratio between PbX_6 octahedra and A-site cations.[51] The increase in the cationic charge of lead ions will contribute to tightening halides and shrinking the PbX_6 octahedral volume, leading to the enhancement of phase stability. This observation implies that 0D/3D heterostructure has a positive effect on the 3D phase stability enhancement.

The green PeLEDs were fabricated to study the effect of one-step self-organized 0D $Cs_{4-x}K_xPbBr_6$/3D $CsPbBr_3$ heterostructure carrier confinement strategy on the photoelectric performance. Figure 6a shows the schematic diagram and cross-sectional SEM image of the PeLED device structure, which consists of glass/indium tin oxide (ITO)/PEDOT:PSS/Perovskite/1,3,5-tris(1-phenyl-1H-benzimidazol-2-yl)benzene (TPBi)/LiF/Al. The ultraviolet photoelectron spectroscopy (UPS) and UV-visible spectroscopy methods (Figure S11) were employed to determine the energy level of the corresponding perovskite films. The corresponding schematics of the flat-band energy

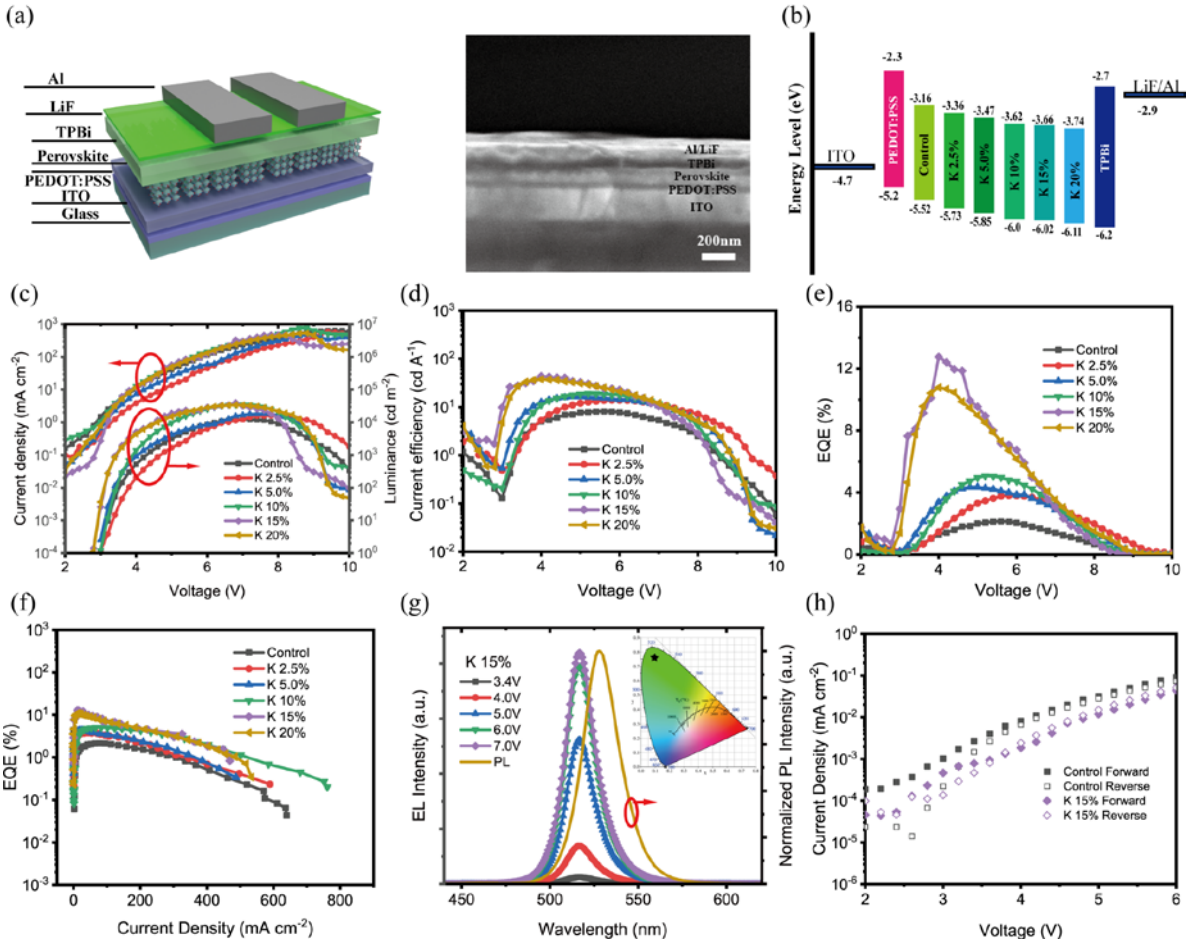

Figure 6. (a) Schematic and cross-sectional SEM image of the PeLED device structure, (b) Energy band alignment of each functional layer in the PeLED device, (c) J-V-L, (d) CE-V, (e) EQE-V, (f) CE-J characteristic curves, (g) PL spectra and EL spectra of K15% 0D/3D heterostructure PeLEDs under varying voltage bias, (h) the CIE coordinates of the corresponding PeLED, (i) J-V hysteresis of PeLEDs based on control (3D) perovskite and K15% (0D/3D) heterostructure perovskite films.

This journal is © The Royal Society of Chemistry 20xx

Please do not adjust margins

Please do not adjust margins

level diagram of the device are shown in Figure 6(b). The current density-voltage (J-V), luminance-voltage (V-L), current efficiency-voltage (CE-V) curves, EQE-voltage (EQE-V), and EQE-current density curves (EQE-CD) of the 3D $CsPbBr_3$ and 0D/3D heterostructure based PeLEDs are shown in Figure 6c, d, e, and f, respectively. As expected, the device based on the $CsPbBr_3/Cs_{4-x}K_xPbBr_6$ heterostructure EML shows significantly improved performance. According to the J-V-L curves shown in Figure 6(c), the K15% and K20% 0D/3D heterostructure PeLEDs exhibit the lowest turn-on voltage around 2.8 V, which is slightly higher than the optical bandgap of the emitting material. The turn-on voltage indicates the lowest voltage required for radiative recombination in the PeLEDs. Additionally, the 0D/3D perovskite PeLEDs based on K15% perovskite film achieved the maximum luminance (39400 cd m^{-2}), which is around three times higher than that of the pristine 3D $CsPbBr_3$ one (12500 cd m^{-2}).

Apart from the I-V-L characteristics, the optoelectronic conversion efficiency of these PeLEDs was also measured. The efficiency of all devices based on 0D/3D perovskite is significantly enhanced compared to that of the control one. The maximum current efficiency increased to 43.7 cd A^{-1} from 8.2 cd A^{-1}, obtained for the K15 0D/3D perovskite films (Figure 6d). Meanwhile, the maximum EQE significantly increase from 2.1% to 12.8%, benefiting from the preservation of high PLQY for the K15 0D/3D perovskite film (Figure 6e, 6f). The combination of improved PLQY and low trap density contribute to the improvement of PeLEDs efficiency, indicating the effective charge carrier recombination in 3D perovskite phase for the 0D/3D carrier confinement heterostructure. The details of the 3D $CsPbBr_3$ and 0D/3D heterostructure-based PeLEDs are summarized in Table 1. Furthermore, the EL spectra reveal a slight blue shift to 516 nm, comparing with the PL emission at 527 nm for the K15% 0D/3D heterostructure perovskite films, shown in Figure 6(g).[52] These fabricated devices demonstrated symmetric and narrow EL peaks with a full-width at half-maximum (FWHM) of 20 nm. As the bias voltage increases from 3.4 to 7 V, the EL peak position and FWHM remain unchanged, suggesting the high color purity. According to the CIE 1931 standard color-matching functions, the emitted green K15% 0D/3D heterostructure PeLEDs can be indexed by (x, y) chromaticity coordinates as (0.11, 0.77) given in the inset of Figure 6 (g). Moreover, in order to investigate the photocurrent hysteresis in our PeLEDs, the current density-voltage (J-V) curves in various scanning directions were conducted and shown in Figure 6(h). It was found that the K15% 0D/3D heterostructure PeLEDs show a relatively low hysteresis, demonstrating that the ion migration can be suppressed.

Table 1. Summary of the 3D $CsPbBr_3$ and 0D/3D heterostructures-based perovskite LEDs

KBr ratio	V_T (V)	EL peak (nm)	Max. L. (cd m^{-2})	Max. CE (cd A^{-1})	Max. EQE (%)	FWHM (nm)	CIE
0%	3.2	520	12500	8.2	2.1	22	(0.140,0.771)
2.5%	3.0	518	16400	13.9	3.8	23	(0.124,0.765)
5.0%	3.0	517	18300	16.3	4.4	22	(0.113,0.767)
10%	3.0	516	34900	18.9	5.1	22	(0.113,0.769)
15%	2.8	516	39400	43.7	12.8	20	(0.108,0.769)
20%	2.8	516	33900	37.4	10.8	21	(0.104,0.761)

Conclusions

In summary, we reported a facial approach to form 0D/3D mixed-dimensional self-assembled heterostructure perovskite film to significantly improve the efficiency of $CsPbBr_3$-based PeLEDs. By adding KBr in perovskite precursor, the $Cs_{4-x}K_xPbBr_6/CsPbBr_3$ perovskite type-I heterostructure film can be achieved. With this unique heterostructure, the grain boundary defects passivation can be observed, which is responsible for improved PLQY. Moreover, the formation of this 0D/3D perovskite heterostructure is conducive to confine the charge carriers and boost the recombination efficiency of electrons and holes in the 3D phase. More importantly, the PeLEDs utilizing 15% KBr-based 0D/3D heterostructure as emitter layer exhibited a high brightness of 39400 cd m^{-2} and a relatively high external quantum efficiency of 12.8 % which is more than six times higher than the pristine one (2.1%). Our results reveal the relationship between 0D/3D carrier centralization heterostructure and PeLEDs device performance. The heterostructure formation will serve as a feasible and effective tool for developing another $CsPbBr_3$-based perovskite heterostructure, and also can be applied to other potential perovskite systems to break the bottleneck of PeLEDs efficiencies further, simultaneously.

Author Contributions

L.C.Z. fabricated and characterised the devices and carry out the most measurement. S.L. supervised the work. L.L.Z. performed the SEM measurements and the DFT. Y.L. performed the AFM measurements. H.R. performed the TA measurements. L.C.Z., L.L.Z., Y.L., H.R., M.L., and S.L. analysed and discussed the experimental results. All authors contributed to writing the article.

Conflicts of interest

There are no conflicts to declare.

Acknowledgements

This work was financially supported by the Hong Kong Polytechnic University grant (1-ZVGH).

Notes and references

1 M. Payandeh, V. Ahmadi, F. Arabpour Roghabadi, P. Nazari, F. Ansari, P. Brenner, R. Bäuerle, M. Jakoby, U. Lemmer, I. A. Howard, B. S. Richards, U. W. Paetzold and B. Abdollahi Nejand, *ACS Appl. Mater. Interfaces*, 2020, **12**, 11428-11437.

2 X. Zhang, W. Wang, B. Xu, H. Liu, H. Shi, H. Dai, X. Zhang, S. Chen, K. Wang and X. W. Sun, *ACS Appl. Mater. Interfaces*, 2018, **10**, 24242-24248.

3 B. Zhao, S. Bai, V. Kim, R. Lamboll, R. Shivanna, F. Auras, J. M. Richter, L. Yang, L. Dai, M. Alsari, X.-J. She, L. Liang, J. Zhang, S. Lilliu, P. Gao, H. J. Snaith, J. Wang, N. C. Greenham, R. H. Friend and D. Di, *Nat. Photonics*, 2018, **12**, 783-789.

4 Z.-K. Tan, R. S. Moghaddam, M. L. Lai, P. Docampo, R. Higler, F. Deschler, M. Price, A. Sadhanala, L. M. Pazos, D.

Please do not adjust margins

Please do not adjust margins

Credgington, F. Hanusch, T. Bein, H. J. Snaith and R. H. Friend, *Nat. Nanotechnology*, 2014, **9**, 687-692.
5 Y.-H. Kim, S. Kim, A. Kakekhani, J. Park, J. Park, Y.-H. Lee, H. Xu, S. Nagane, R. B. Wexler, D.-H. Kim, S. H. Jo, L. Martínez-Sarti, P. Tan, A. Sadhanala, G.-S. Park, Y.-W. Kim, B. Hu, H. J. Bolink, S. Yoo, R. H. Friend, A. M. Rappe and T.-W. Lee, *Nat. Photonics*, 2021, **15**, 148-155.
6 X. Wang, Z. Bao, Y.-C. Chang and R.-S. Liu, *ACS Energy Lett.*, 2020, **5**, 3374-3396.
7 Z. Bao, Y.-J. Tseng, W. You, W. Zheng, X. Chen, S. Mahlik, A. Lazarowska, T. Lesniewski, M. Grinberg, C. Ma, W. Sun, W. Zhou, R.-S. Liu and J. P. Attfield, *J. Phys. Chem. Lett.*, 2020, **11**, 7637-7642.
8 H. Wang, X. Zhang, Q. Wu, F. Cao, D. Yang, Y. Shang, Z. Ning, W. Zhang, W. Zheng, Y. Yan, S. V. Kershaw, L. Zhang, A. L. Rogach and X. Yang, *Nat. Commun.*, 2019, **10**, 665.
9 T. Xu, Y. Meng, M. Wang, M. Li, M. Ahmadi, Z. Xiong, S. Yan, P. Chen and B. Hu, *J. Mater. Chem. C*, 2019, **7**, 8287-8293.
10 T.-H. Han, J.-W. Lee, Y. J. Choi, C. Choi, S. Tan, S.-J. Lee, Y. Zhao, Y. Huang, D. Kim and Y. Yang, *Adv. Mater.*, 2020, **32**, 1905674.
11 J. Yan, G. Croes, A. Fakharuddin, W. Song, P. Heremans, H. Chen and W. Qiu, *Adv. Opt. Mater.*, 2019, **7**, 1900465.
12 Y. Li, J. Zhu, Y. Huang, F. Liu, M. Lv, S. Chen, L. Hu, J. Tang, J. Yao and S. Dai, *RSC Adv.*, 2015, **5**, 28424-28429.
13 Z. Xiao, R. A. Kerner, L. Zhao, N. L. Tran, K. M. Lee, T.-W. Koh, G. D. Scholes and B. P. Rand, *Nat. Photonics*, 2017, **11**, 108-115.
14 B. Hwang, Y. Park and J.-S. Lee, *J. Mater. Chem. C*, 2021, **9**, 110-116.
15 L. Dou, J. You, Z. Hong, Z. Xu, G. Li, R. A. Street and Y. Yang, *Adv. Mater.*, 2013, **25**, 6642-6671.
16 S. H. Park, A. Roy, S. Beaupré, S. Cho, N. Coates, J. S. Moon, D. Moses, M. Leclerc, K. Lee and A. J. Heeger, *Nat. Photonics*, 2009, **3**, 297-302.
17 Z. Wang, Q. Lin, F. P. Chmiel, N. Sakai, L. M. Herz and H. J. Snaith, Nat. Energy, 2017, **2**, 17135.
18 J. Xu, W. Huang, P. Li, D. R. Onken, C. Dun, Y. Guo, K. B. Ucer, C. Lu, H. Wang, S. M. Geyer, R. T. Williams and D. L. Carroll, *Adv. Mater.*, 2017, **29**, 1703703.
19 F. Bai, J. Zhang, Y. Yuan, H. Liu, X. Li, C.-C. Chueh, H. Yan, Z. Zhu and A. K. Y. Jen, *Adv. Mater.*, 2019, **31**, 1904735.
20 A. Younis, L. Hu, P. Sharma, C. -H. Lin, Y. Mi, X. Guang, D. Zhang, Y. Wang, T. He, X. Liu, B. Shabbir, S. Huang, J. Seidel and T. Wu, *Adv. Funct. Mater.*, 2020, **30**, 2002948.
21 D.-K. Lee, Y. Shin, H. J. Jang, J.-H. Lee, K. Park, W. Lee, S. Yoo, J. Y. Lee, D. Kim, J.-W. Lee and N.-G. Park, *ACS Energy Lett.*, 2021, **6**, 1821-1830.
22 F. Zhang, B. Cai, J. Song, B. Han, B. Zhang and H. Zeng, *Adv. Funct. Mater.*, 2020, **30**, 2001732.
23 G. Kresse and J. Hafner, *Phys. Rev. B*, 1994, **49**, 14251.
24 G. Kresse and J. Furthmüller, *Phys. Rev. B*, 1996, **54**, 11169.
25 G. Kresse and D. Joubert, *Phys. Rev. B*, 1999, **59**, 1758.
26 B. Hammer, L. B. Hansen and J. K. Nørskov, *Phys. Rev. B*, 1999, **59**, 7413.
27 P. E. Blöchl, *Phys. Rev. B*, 1994, **50**, 17953.
28 H. J. Monkhorst and J. D. Pack, *Phys. Rev. B*, 1976, **13**, 5188.
29 H. Lin, C. Zhou, Y. Tian, T. Siegrist and B. Ma, *ACS Energy Lett.*, 2018, **3**, 54-62.
30 G. Bergerhoff and O. Schmitz-Dumont, *Z. Anorg. All. Chem.*, 1956, **284**, 10-19.
31 Y. Shang, G. Li, W. Liu and Z. Ning, *Adv. Funct.Mater.*, 2018, **28**, 1801193.
32 A. Kanwat, N. Yantara, Y. F. Ng, T. J. N. Hooper, P. J. S. Rana, B. Febriansyah, P. C. Harikesh, T. Salim, P. Vashishtha, S. G. Mhaisalkar and N. Mathews, *ACS Energy Lett.*, 2020, **5**, 1804-1813.
33 F. Cao, D. Yu, W. Ma, X. Xu, B. Cai, Y. M. Yang, S. Liu, L. He, Y. Ke, S. Lan, K.-L. Choy and H. Zeng, *ACS Nano*, 2020, **14**, 5183-5193.
34 L. Nasi, D. Calestani, F. Mezzadri, F. Mariano, A. Listorti, P. Ferro, M. Mazzeo and R. Mosca, *Front. Chem.*, 2020, **8**, 313.
35 M. Nikl, K. Nitsch, E. Mihokova, K. Polak, P. Fabeni, G. Pazzi, M. Gurioli, R. Phani, S. Santucci and A. Scacco, *Radiat. Eff. Defect. S.*, 1999, **150**, 341-345.
36 M. I. Saidaminov, J. Almutlaq, S. Sarmah, I. Dursun, A. A. Zhumekenov, R. Begum, J. Pan, N. Cho, O. F. Mohammed and O. M. Bakr, *ACS Energy Lett.*, 2016, **1**, 840-845.
37 Y. Zhang, M. I. Saidaminov, I. Dursun, H. Yang, B. Murali, E. Alarousu, E. Yengel, B. A. Alshankiti, O. M. Bakr and O. F. Mohammed, *J. Phys. Chem. Lett.*, 2017, **8**, 961-965.
38 L. N. Quan, R. Quintero-Bermudez, O. Voznyy, G. Walters, A. Jain, J. Z. Fan, X. Zheng, Z. Yang and E. H. Sargent, *Adv. Mater.*, 2017, **29**, 1605945.
39 S.-H. Turren-Cruz, M. Saliba, M. T. Mayer, H. Juárez-Santiesteban, X. Mathew, L. Nienhaus, W. Tress, M. P. Erodici, M.-J. Sher, M. G. Bawendi, M. Grätzel, A. Abate, A. Hagfeldt and J.-P. Correa-Baena, *Energy Environ. Sci.*, 2018, **11**, 78-86.
40 D. J. Kubicki, D. Prochowicz, A. Hofstetter, S. M. Zakeeruddin, M. Grätzel and L. Emsley, *J. Am. Chem. Soc.*, 2017, **139**, 14173-14180.
41 N. Li, L. Song, Y. Jia, Y. Dong, F. Xie, L. Wang, S. Tao and N. Zhao, *Adv. Mater.*, 2020, **32**, 1907786.
42 Z. Gan, F. Zheng, W. Mao, C. Zhou, W. Chen, U. Bach, P. Tapping, T. W. Kee, J. A. Davis, B. Jia and X. Wen, *Nanoscale*, 2019, **11**, 14676-14683.
43 S. Park, M. N. An, G. Almeida, F. Palazon, D. Spirito, R. Krahne, Z. Dang, L. De Trizio and L. Manna, *Nanoscale*, 2019, **11**, 18739-18745.
44 Z. Li, X. Liu, J. Xu, S. Yang, H. Zhao, H. Huang, S. Liu and J. Yao, *J. Mater. Chem. C*, 2020, **8**, 6977-6987.
45 J. C. de Mello, H. F. Wittmann and R. H. Friend, *Adv. Mater.*, 1997, **9**, 230-232.
46 T. Xuan, S. Lou, J. Huang, L. Cao, X. Yang, H. Li and J. Wang, *Nanoscale*, 2018, **10**, 9840-9844.
47 X. Li, Y. Wu, S. Zhang, B. Cai, Y. Gu, J. Song and H. Zeng, *Adv. Funct. Mater.*, 2016, **26**, 2435-2445.
48 Y. Ling, L. Tan, X. Wang, Y. Zhou, Y. Xin, B. Ma, K. Hanson and H. Gao, *J. Phys.Chem. Lett.*, 2017, **8**, 3266-3271.
49 H. Shibata, *Jpn. J. Appl. Phys.*, 1998, **37**, 550-553.
50 M. Schulzendorf, A. Hinaut, M. Kisiel, R. Jöhr, R. Pawlak, P. Restuccia, E. Meyer, M. C. Righi and T. Glatzel, *ACS Nano*, 2019, **13**, 5485-5492.
51 Z. Li, M. Yang, J.-S. Park, S.-H. Wei, J. J. Berry and K. Zhu, *Chem. Mater.*, 2016, **28**, 284-292.
52 L. Zhang, X. Yang, Q. Jiang, P. Wang, Z. Yin, X. Zhang, H. Tan, Y. Yang, M. Wei, B. R. Sutherland, E. H. Sargent and J. You, *Nat. Commun.*, 2017, **8**, 15640.

 This journal is © The Royal Society of Chemistry 20xx

Please do not adjust margins